Journal of Alloys and Compounds 749 (2018) 473–480

Contents lists available at ScienceDirect

Journal of Alloys and Compounds

journal homepage: http://www.elsevier.com/locate/jalcom

Enhanced hydrogen evolution via interlaced Ni_3S_2/MoS_2 heterojunction photocatalysts with efficient interfacial contact and broadband absorption

Shaohui Guo [a, b, c, 1], Lin Yang [a, b, 1], Yuanyuan Zhang [a, b], Zhixiang Huang [d], Xingang Ren [d], Wei E.I. Sha [e], Xuanhua Li [a, b, c, *]

[a] State Key Laboratory of Solidification Processing, Center for Nano Energy Materials, School of Materials Science and Engineering, Northwestern Polytechnical University and Shaanxi Joint Lab of Graphene (NPU), Xi'an, 710072, China
[b] Research & Development Institute of Northwestern Polytechnical University in Shenzhen, China
[c] State Key Laboratory of Silicate Materials for Architectures, Wuhan University of Technology, China
[d] Key Laboratory of Intelligent Computing & Signal Processing, Ministry of Education, Anhui University, No. 3 Feixi Road, Hefei, Anhui Province, 230039, China
[e] College of Information Science & Electronic Engineering, Zhejiang University, Hangzhou, China

ARTICLE INFO

Article history:
Received 4 December 2017
Received in revised form
21 March 2018
Accepted 26 March 2018
Available online 27 March 2018

Keywords:
Ni_3S_2
MoS_2
Interfacial contact
Heterostructure
Photocatalytic hydrogen evolution

ABSTRACT

The development of transition-metal sulfides, such as nickel sulfides (e.g., Ni_3S_2), as catalysts for the hydrogen evolution reaction is one potential solution to environmental pollution and energy crisis. However, its limited utilization of visible light and high recombination ratio of photoinduced electron–hole pairs suppress its photocatalytic activity. The key issue in improving photocatalytic efficiency lies in fabricating a p–n heterojunction with efficient interfacial contact and broadband absorption. Here, we developed a method for fabricating an interlaced Ni_3S_2/MoS_2 heterostructure with close interfacial contact. In our fabrication approach, a porous Ni_3S_2 scaffold is prepared by chemical vapor deposition and a hydrothermal method is used to prepare a Ni_3S_2/MoS_2 photocatalyst with close interfacial contact. The numerous interfaces of the interlaced Ni_3S_2/MoS_2 heterostructures promote effective electron–hole pair separation and facilitate electron transfer. Meanwhile, the hybrid Ni_3S_2/MoS_2 nanostructures favor broadband absorption extending from 300 to 800 nm. As a result, the hybrid Ni_3S_2/MoS_2 exhibits a remarkable rate of hydrogen evolution (540.75 μmol g^{-1} h^{-1}), which is 5.71 and 3.89 times greater than those of pure Ni_3S_2 and MoS_2, respectively, under otherwise identical conditions. The results of this work are significant for developing promising transition-metal sulfide heterostructures in the field of hydrogen evolution by photocatalytic water splitting.

1. Introduction

Solar energy and hydrogen are clean and renewable energy resources that may be viable alternatives for alleviating the environmental problems and energy crisis associated with fossil fuels. Photocatalytic water splitting provides a promising and effective path for producing hydrogen using solar energy [1–3]. Consequently, the development of semiconductor photocatalysts has become an active research topic [4,5]. However, the design and construction of new semiconductor nanostructures are capable of broadband light harvesting and effective electron–hole pair separation as well as outstanding electron transfer remains a formidable challenge [6,7]. The synthesis of efficient and low-cost photocatalysts will promote their practical application.

Numerous reports have indicated that transition-metal sulfide semiconductor materials are good photocatalyst candidates [8,9]. Among the transition-metal sulfides, nickel sulfides include numerous species that can catalyze the hydrogen evolution reaction, such as, NiS, NiS_2, Ni_3S_2, and Ni_3S_4 [10–15]. Nickel subsulfide (Ni_3S_2), a metallic sulfide semiconductor [16], exhibits good optical and electrical properties in addition to certain limited photocatalytic properties. However, its limited utilization of visible light and its high recombination ratio of photoinduced electron–hole pairs suppress its photocatalytic activity. The unsatisfactory photocatalytic performance of simple Ni_3S_2 has led to the development of several strategies for increasing its photocatalytic efficiency [17,18]. For example,

* Corresponding author. State Key Laboratory of Solidification Processing, Center for Nano Energy Materials, School of Materials Science and Engineering, Northwestern Polytechnical University and Shaanxi Joint Lab of Graphene (NPU), Xi'an, 710072, China.
E-mail address: lixh32@nwpu.edu.cn (X. Li).
[1] Shaohui Guo and Lin Yang equally contributed to this work.

https://doi.org/10.1016/j.jallcom.2018.03.329
0925-8388/

Lin et al. combined Erythrosin Yellowish (ErY) as a sensitizer, carbon nanotubes, and Au nanoparticles with Ni_3S_2 to improve its photocatalytic activity [19]. However, the introduction of Au nanoparticles increases the cost, and ErY is an environmental pollutant.

An alternative approach to improve the photocatalytic performance of photocatalysts is to form a semiconductor heterojunction [20–23]. Heterostructured photocatalysts broaden the scope of light harvesting. Furthermore, band alignment between the two semiconducting materials of a heterojunction results in a built-in field at the interface of the junction for the spatial separation of photoinduced electron–hole pairs and the transport of electrons and holes. However, the architectural design of heterostructures should be improved. The issue of fabricating a heterojunction with efficient interfacial contact is a key obstacle to improve photocatalytic efficiency. MoS_2, a low-cost few-layered molybdenum disulfide, has attracted extensive attention as a hydrogen evolution reaction catalyst. Combining MoS_2 as a catalyst with traditional photocatalysts can result in enhanced solar energy absorption in the visible region. Furthermore, if the band states of the photocatalysts and MoS_2 match each other, the heterostructure assists in electron transport and in retarding charge recombination. Since of its advantageous optical and electronic properties, MoS_2 can ultimately be used to improve photocatalytic activity.

In this work, a facile method is developed for fabricating an interlaced Ni_3S_2/MoS_2 heterostructure with intimate interfacial contact. In this approach, Ni foam is sulfurized in a chemical vapor deposition (CVD) system and forms a porous Ni_3S_2 scaffold. A molybdenum and sulfur precursor solution then comes into contact with the scaffold sufficiently to enable MoS_2 growth via a hydrothermal reaction. The optical absorption region of the Ni_3S_2/MoS_2 heterostructures ranges from 300 to 800 nm. The numerous interfaces of the interlaced Ni_3S_2/MoS_2 heterostructures promote effective electron–hole pair separation and facilitate electron transfer. As a result, the photocatalytic hydrogen evolution rate of the Ni_3S_2/MoS_2 photocatalyst is 5.71 (3.89) times higher than that of pure Ni_3S_2 (MoS_2) under the same test conditions. We also obtained a series of measurements to elucidate the mechanism of photocatalysis.

2. Experimental section

2.1. Synthesis of the Ni3S2, MoS2, and Ni3S2/MoS2 heterostructure

The Ni_3S_2 was synthesized through a CVD method. Ni foam ($2 \times 2\ cm^2$) was vulcanized by sulfur powder in a 100 sccm argon atmosphere tube furnace at 700 °C and 250 Pa for 10 min. The Ni_3S_2/MoS_2 heterostructure was obtained via a hydrothermal reaction. As-synthesized Ni_3S_2 was added to a 50 mL Teflon-lined stainless steel autoclave to which Na_2MoO_4 (3.0 mmol) and L-cysteine solution (6.0 mmol) were added; the Ni_3S_2/MoS_2 heterostructure was subsequently obtained after the autoclave was heated at 200 °C for 16 h and allowed to cool to room temperature naturally. The product was precipitated by centrifugation at 6000 rpm for 10 min. Single MoS_2 was prepared though hydrothermal method, which is consistent with the preparation condition of MoS_2 in heterojunction. We added the Na_2MoO_4 (3.0 mmol) and L-cysteine solution (6.0 mmol) into a 50 mL Teflon-lined stainless steel autoclave. Subsequently, the autoclave was heated at 200 °C for 16 h and allowed to cool to room temperature naturally. The product was precipitated by centrifugation at 6000 rpm for 10 min. Finally, the three products were separately dispersed in distilled water by ultrasonication for 30 min.

2.2. Morphology and structural characterization

The morphologic micrographs of the Ni_3S_2/MoS_2 heterostructure were obtained using a scanning electron microscope (FEI NOVA) and a transmission electron microscope (FEI Tecnai F30G2). An X-ray diffractometer (PANalytical B.V., Cu-K_α radiation, $\lambda = 1.54178$ Å) was used for phase analysis. XPS (ESCALAB 250Xi) was performed to identify the elements present at the surface and their oxidation states. The optical properties of the samples were characterized by UV–vis spectrophotometry (PerkinElmer Lambda 35 UV-VIS) and Raman spectrometry (Renishaw inVia) with a 532 nm excitation laser with a spot diameter of 1 μm. The photoluminescence emission spectra at room temperature were acquired using a fluorescence spectrometer (FLS 980) with a 325 nm Xe arc lamp and a 5 nm slit width.

2.3. Photocatalytic activity

H_2 evolution reactions were carried out in a 40 mL gas-tight glass system under vacuum. A 150 W Xe arc lamp served as the light source and was placed 10 cm from the reactor, which was mounted with a fan for dissipating excessive heat. During the photocatalytic reaction with 0.1 mol L^{-1} $Na_2S \cdot 9H_2O$ and 0.1 mol L^{-1} Na_2SO_3 as hole sacrificial reagents, 0.05 g of photocatalyst was dispersed in distilled water (40 mL) and kept in an ultrasonic device for 30 min. Then, in order to compare the photocatalytic ability of Ni_3S_2/MoS_2 heterojunction with single Ni_3S_2 and MoS_2, we added the same mass (0.05 g) of three kinds of photocatalyst to conduct the hydrogen evolution reaction. After every 20 min cycle under light irradiation, the gas was transferred into a sample loop via a peristaltic pump and subsequently analyzed by gas chromatography on a gas chromatograph (Shimadzu GC-2014c) equipped with a thermal conductivity detector [24,25].

2.4. Photoelectrochemical measurements

Photoelectrochemical experiments were conducted on a Chenhua 760 electrochemical workstation using a three-electrode reactor with Na_2SO_4 solution (0.5 mol L^{-1}) as the electrolyte. Pt foil served as the counter electrode and an Ag/AgCl electrode served as the reference electrode. A 100 μL sample solution was coated onto the surface of a 1 cm^2 fluorine doped tin oxide (FTO) substrate and heated at 50 °C for 10 min; this electrode was subsequently used as the working electrode. In the photoelectrochemical experiments, a 150 W Xe lamp irradiated the working electrode. The electrochemical impedance spectroscopy (EIS) and Mott–Schottky measurements were conducted in light at a frequency of 10,000 Hz. The photocurrent was measured by chronoamperometry.

3. Results and discussion

The Ni_3S_2/MoS_2 heterostructures were fabricated via the following method. As shown in Scheme 1, the Ni_3S_2 nanostructure was generated on a Ni foam through sulfuration procedure by the CVD method; MoS_2 was then grown along the Ni_3S_2 nanostructure, resulting in the formation of the Ni_3S_2/MoS_2 heterostructure through a hydrothermal procedure, in which L-cysteine and Na_2MoO_4 were used as sulfur and molybdenum precursors, respectively. Since the Ni_3S_2 nanostructure was fabricated on Ni foam, it could be used as a scaffold. The subsequent decorated MoS_2 achieved intimate contact with the Ni_3S_2 scaffold, resulting in efficient interfacial contact.

X-ray diffraction (XRD) was used to characterize the crystal structure of the Ni_3S_2 and the Ni_3S_2/MoS_2 heterostructure. XRD patterns for the Ni_3S_2 and Ni_3S_2/MoS_2 samples are shown in Fig. 1(a). These data match those in PDF card 44-1418 (Ni_3S_2) and PDF card 01-075-1539 (MoS_2). The XRD pattern of the Ni foam after CVD vulcanization shows peaks at $2\theta = 21.61°$ and 30.92°, which

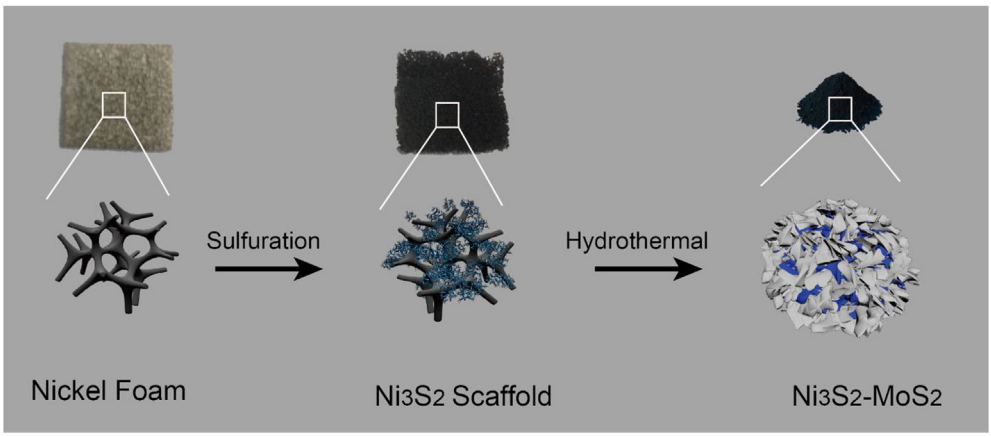

Scheme 1. The fabrication process of interlaced Ni_3S_2/MoS_2 heterostructures.

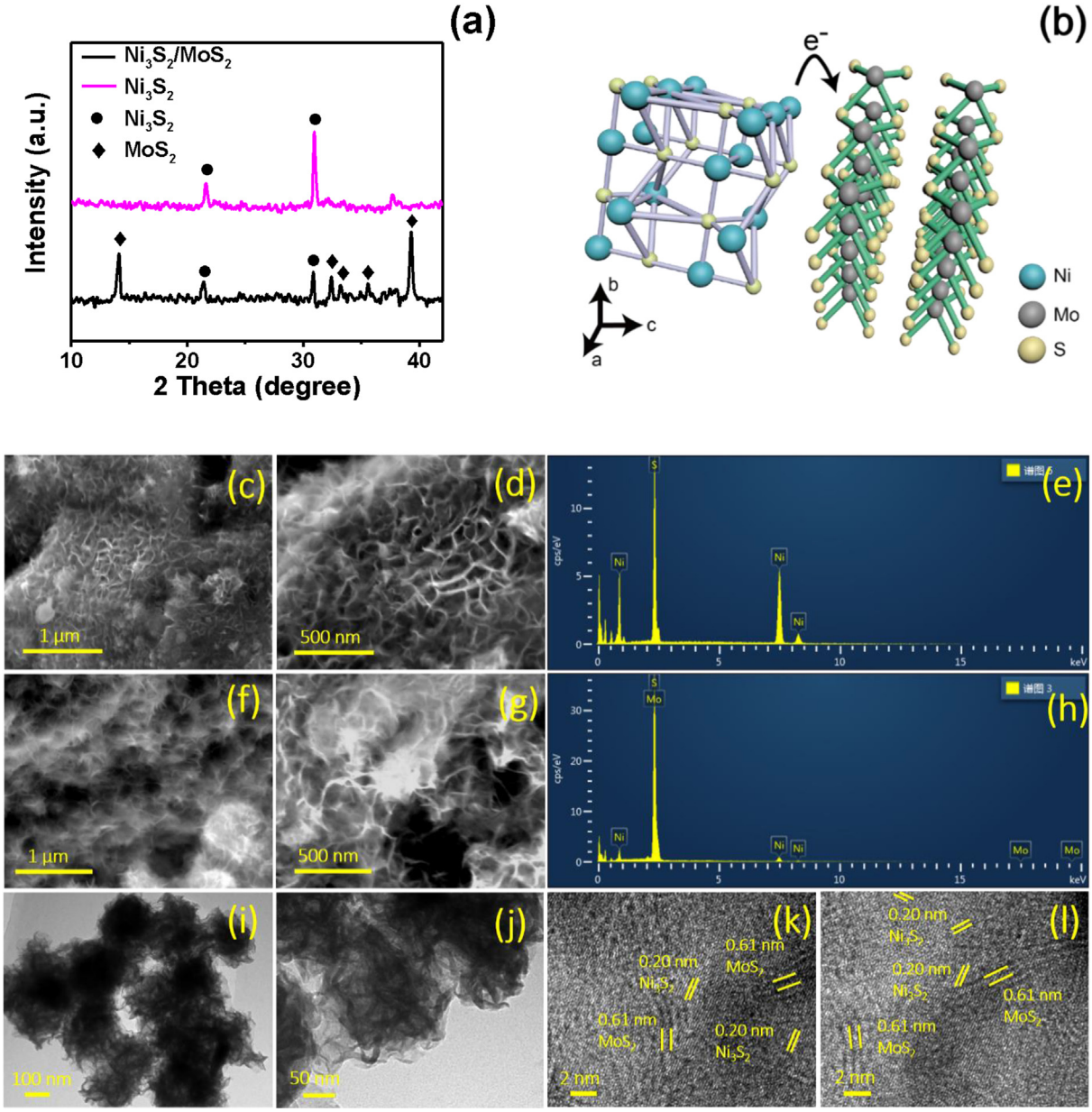

Fig. 1. (a) XRD patterns for the Ni_3S_2 and Ni_3S_2/MoS_2 samples; (b) Scheme of the contact type of the interlaced Ni_3S_2/MoS_2 heterostructure; (c, d) SEM images of the Ni_3S_2; e) EDXA of the Ni_3S_2; (f, g) SEM images of the Ni_3S_2/MoS_2 heterostructures; (h) EDXA of the Ni_3S_2/MoS_2 heterostructures; (i, j) TEM images of the Ni_3S_2/MoS_2 heterostructure; (k, l) TEM images at the interface of the Ni_3S_2/MoS_2 heterostructure.

originate from the (101) and (110) planes of Ni_3S_2, respectively. In the XRD pattern of the hybrid structure, apart from the peaks assigned to Ni_3S_2, the peaks at $2\theta = 14.13^\circ$ and 39.51° are assigned to the (002) and (103) planes of MoS_2 (2H-MoS_2). Thus, the Ni_3S_2/MoS_2 heterostructures comprise Ni_3S_2 and MoS_2. The morphology of the samples was characterized by scanning electron microscopy (SEM) and transmission electron microscopy (TEM). As shown in Fig. 1(c) and (d), the morphology of the Ni_3S_2 obtained by sulfurization of Ni foam comprises many thin nanosheets, which tend to grow on the Ni foam at a certain oblique angle and are interconnected. Energy-dispersive X-ray analysis (EDXA) confirms that only Ni and S are present in the nanostructures (Fig. 1(e)). SEM images of the Ni_3S_2/MoS_2 heterostructures after the introduction of MoS_2 are shown in Fig. 1(f) and (g). The Ni_3S_2 is covered with MoS_2 nanosheets that grow densely on the surface of the Ni_3S_2. Meanwhile, EDXA also confirms that Ni, Mo, and S are present in the Ni_3S_2/MoS_2 heterostructure (Fig. 1(h)). To further explore the detailed characteristics of the heterostructures, we used TEM to characterize the samples. Fig. 1(i) and (j) show some hybrid spherical particles with a diameter of approximately 200 nm. The two materials are interwoven with each other and form interlaced Ni_3S_2/MoS_2 heterostructures with intimate interfacial contact. Furthermore, TEM images of the interfaces are shown in Fig. 1(k) and (l). Two distinct lattice fringes belonging to MoS_2 and Ni_3S_2, respectively, are revealed. An interlayer spacing of 0.61 nm is observed, which is assigned to the lattice spacing of the (002) plane of MoS_2 [26,27], whereas the observed lattice spacing of 0.20 nm corresponds to the (202) facet of Ni_3S_2 [28]. The MoS_2/Ni_3S_2 heterostructures are constituted by numerous interfaces that consist of comprise the (002) facet of MoS_2 and the neighboring (202) facet of Ni_3S_2. As shown in Fig. 1(b), the MoS_2 and Ni_3S_2 nanosheets align in a specific direction and contact with each other, resulting in the observed interlaced structure.

To further characterize the Ni_3S_2/MoS_2 heterostructure, X-ray photoelectron spectroscopy (XPS) was performed to identify the elemental compositions and the oxidation states of the elements at the surface of the heterostructure. In Fig. 2(a), the XPS survey spectrum show the Ni 2p, Mo 3d, and S 2p signals of the Ni_3S_2/MoS_2 sample. As shown in Fig. 2(b), the Ni 2p XPS spectrum contains two main peaks at 855.9 and 873.6 eV, which are attributed to Ni $2p_{3/2}$ and Ni $2p_{1/2}$, respectively. The other two peaks correspond to the satellite peaks of Ni $2p_{3/2}$ and Ni $2p_{1/2}$.[3] In the Mo 3d region (Fig. 2(c)), the peaks at 228.7 and 232.2 eV are ascribed to Mo $3d_{5/2}$ and Mo $3d_{3/2}$, respectively. This spectrum indicates a +4 oxidation state of Mo and confirms the formation of MoS_2 [26]. Nearby S 2s peaks were fitted at 226.1 and 227.2 eV, corresponding to the two chemical states of S species bonding with Mo and Ni ions. The S 2p spectrum was deconvoluted into four peaks. In Fig. 2(d), the peaks at 162.91 and 163.94 eV are assigned to the S $2p_{3/2}$ and S $2p_{1/2}$ orbitals of divalent sulfide ions (S^{2-}) in MoS_2, and the peaks at 161.81 and 163.81 eV correspond to the S $2p_{3/2}$ and S $2p_{1/2}$ orbitals associated with Ni–S bonding [29].

The amount of visible-light-driven photocatalytic hydrogen gas production of the MoS_2, Ni_3S_2, and the MoS_2/Ni_3S_2 heterostructure

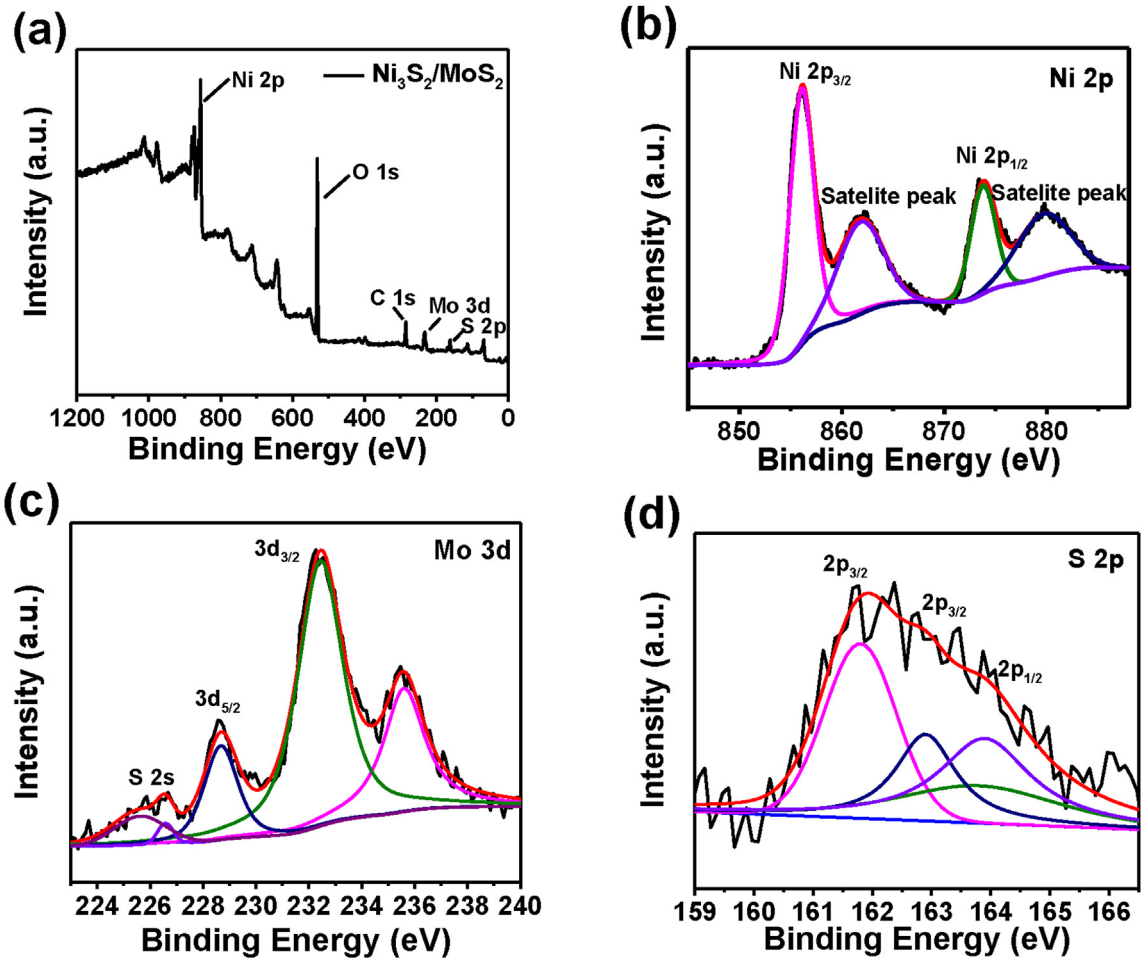

Fig. 2. (a) XPS survey spectrum of the Ni_3S_2/MoS_2 sample; (b) XPS spectrum of Ni 2p; (c) XPS spectrum of Mo 3d; (d) XPS spectrum of S 2p.

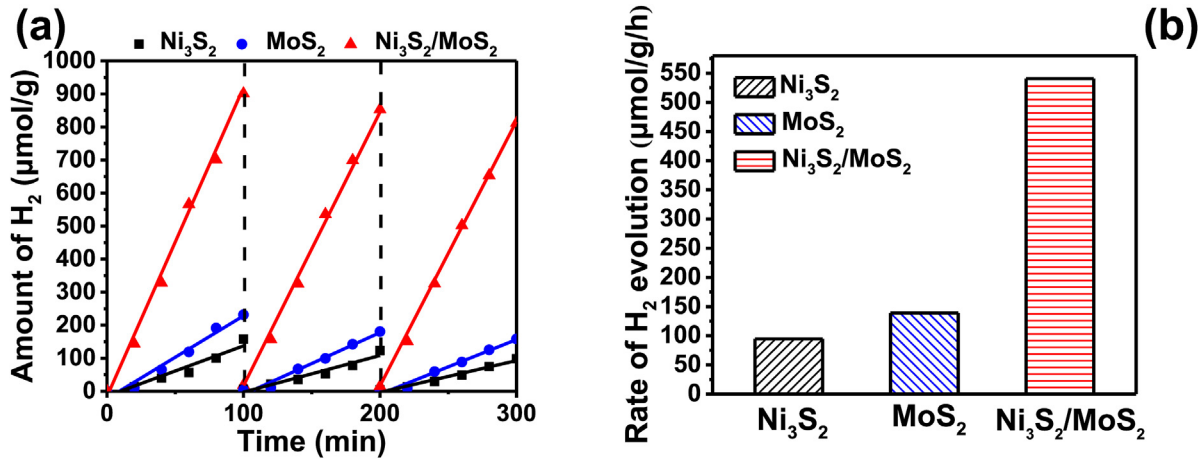

Fig. 3. (a) Time-dependent photocatalytic hydrogen gas production profiles and (b) rates of hydrogen gas production for pure Ni_3S_2, MoS_2, and the interlaced Ni_3S_2/MoS_2 heterostructure.

was tested using Na_2S–Na_2SO_3 as the sacrificial agent. As shown in Fig. 3(a), the amount of hydrogen gas produced when the Ni_3S_2 structure was tested for 100 min in the first cycle was 157.79 μmol g^{-1}, and the amount of hydrogen gas produced when the MoS_2 structure was tested for 100 min in the first cycle was 231.47 μmol g^{-1}. In the case of the hybrid Ni_3S_2/MoS_2 heterostructure, an obvious improvement was observed in the quantity of hydrogen gas production. Specifically, the amount of hydrogen gas production with the Ni_3S_2/MoS_2 heterostructure increased to 901.25 μmol g^{-1}. In addition, after three continuous cycles, the hybrid Ni_3S_2/MoS_2 heterostructure maintained comparable photocatalytic activity. The calculated rates of hydrogen gas production indicate that the interlaced Ni_3S_2/MoS_2 heterostructure (540.75 μmol g^{-1} h^{-1}) manifests a 5.71- and 3.89-fold enhancement in the hydrogen production rate compared with the production rates of the Ni_3S_2 (94.67 μmol g^{-1} h^{-1}) and MoS_2 (138.88 μmol g^{-1} h^{-1}) nanomaterials, respectively (Fig. 3(b)).

To elucidate the mechanism of photocatalysis, we conducted two-part tests involving optical and electrical properties. In terms of the optical process, a photocatalyst should ideally exhibit strong light-harvesting ability to produce a large number of excitons. Fig. 4(a) shows a comparison of the UV–vis absorption spectra of Ni_3S_2, MoS_2, and the Ni_3S_2/MoS_2 heterostructures. In the case of the simple Ni_3S_2 nanosheets, substantial absorption occurs at approximately 430 nm. The UV–vis absorption spectrum of the MoS_2 nanosheets shows two characteristic absorption peaks at 607 and 670 nm [30]. The Ni_3S_2/MoS_2 heterostructure achieves a broad and strong absorption band covering the whole visible spectrum from 300 to 800 nm, which is beneficial for the utilization of solar energy for photocatalysis [31]. The Raman spectra of Ni_3S_2, MoS_2, and the MoS_2/Ni_3S_2 heterostructure further clarify the optical properties of the MoS_2/Ni_3S_2 heterostructure (Fig. 4(b)). The MoS_2 spectrum shows two obvious peaks at 377 and 403 cm^{-1}, which correspond to the E^1_{2g} and A_{1g} Raman modes of MoS_2, respectively. Generally, the in-plane E^1_{2g} mode is attributed to an opposite vibration of the Mo atom with respect to two S atoms, and the A_{1g} mode is related to the out-of-plane vibration of only S atoms along opposite directions. The Raman peaks at 188 cm^{-1}, 202 cm^{-1}, 224 cm^{-1}, 304 cm^{-1}, 325 cm^{-1}, and 350 cm^{-1} are assigned to the vibration modes of Ni_3S_2 [32]. After the formation of Ni_3S_2/MoS_2 heterojunction, Ni_3S_2 nanostructures attach to MoS_2 nanosheets, changing the vibration mode (E^1_{2g} and A_{1g}) of MoS_2 because of interfacial stress between Ni_3S_2 and MoS_2. Thus, the formation of Ni_3S_2/MoS_2 heterojunction leads to the Raman shift of MoS_2 [33].

The excitons' dissociation, transport, and recombination during the electrical transport process were studied. Photoluminescence

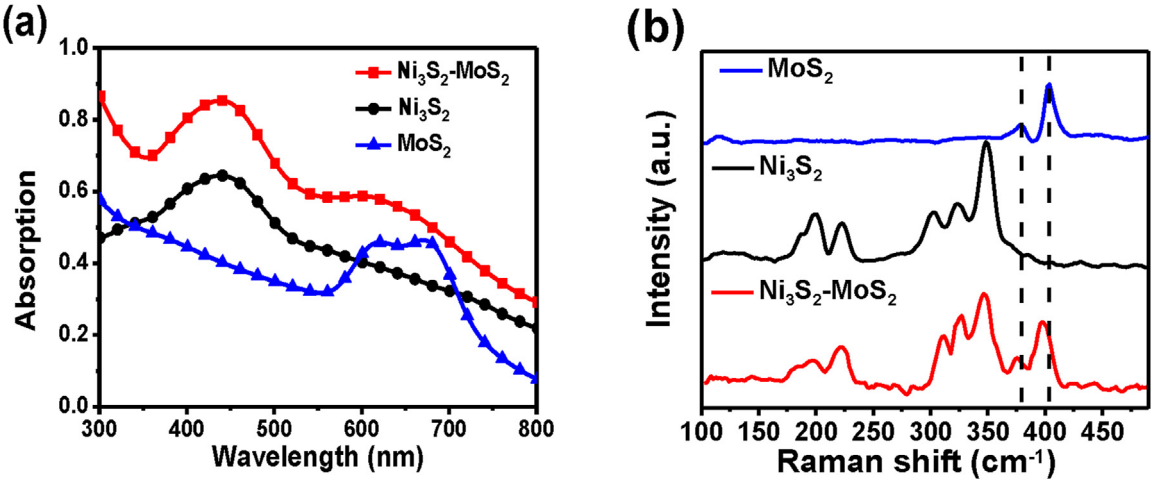

Fig. 4. (a) UV–vis absorption spectra of Ni_3S_2, MoS_2, and the MoS_2/Ni_3S_2 heterostructure; (b) Raman spectra of Ni_3S_2, MoS_2, and the MoS_2/Ni_3S_2 heterostructure.

(PL) emission spectra can illustrate the excitons' separation and the electron–hole pair recombination. Fig. 5(a) shows the PL emission spectra of the samples excited by a 325 nm Xe arc lamp. The characteristic peak at 682 nm is attributed to the bandgap exciton transition for 2H-MoS_2 [34]. The characteristic peaks in the Ni_3S_2 emission spectrum appear at 667, 720, and 741 nm. Remarkably, the overall intensity of the PL emission spectra decreases in the case of the Ni_3S_2/MoS_2 heterostructure, which indicates an improvement in the separation efficiency of electron–hole pairs [35–38]. Researcher has shown that exciton binding energy is approximately equal to the difference between electronic gap and optical gap [39–41]. The exciton binding energies of electron-hole pairs of

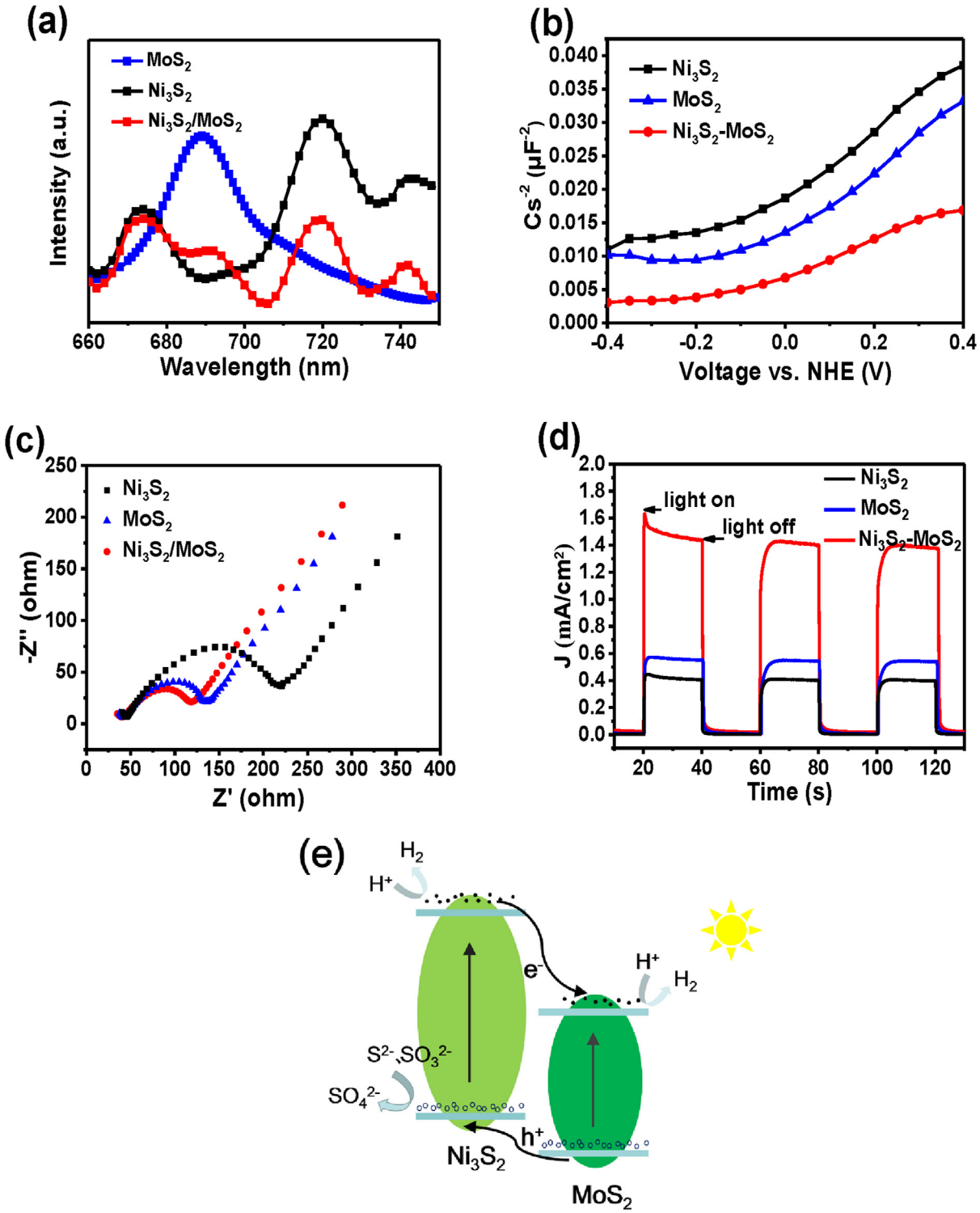

Fig. 5. (a) Photoluminescence emission spectra of the Ni_3S_2, MoS_2, and the interlaced Ni_3S_2/MoS_2 heterostructure; (b) Mott–Schottky plot, (c) the electrochemical impedance data, and (d) chronoamperometry measurement of pure Ni_3S_2 and MoS_2 and the interlaced Ni_3S_2/MoS_2 heterostructure; (e) Scheme of the bandgap alignment between Ni_3S_2 and MoS_2 and the transfer of photo-excited electrons and holes.

Ni_3S_2 and MoS_2 are approximately 0.32 eV and 0.01 eV, respectively. The Mott–Schottky plots of the Ni_3S_2, MoS_2, and the Ni_3S_2/MoS_2 heterostructure are displayed in Fig. 5(b); the curved slope reflects the semiconductor type and the charge carrier density (N_d). The Ni_3S_2, MoS_2, and Ni_3S_2/MoS_2 are n-type semiconductors, and the Ni_3S_2/MoS_2 heterostructure possesses a higher concentration of photoexcited carriers than the individual Ni_3S_2 and MoS_2 materials. Consequently, the higher N_d values of the Ni_3S_2/MoS_2 heterostructure indicate a faster carrier transfer than in the individual Ni_3S_2 and MoS_2, resulting in enhanced water-splitting performance [31]. The electrochemical impedance spectra of the three samples are compared in Fig. 5(c). The arc radius in the Nyquist plots decreases in the order of Ni_3S_2 > MoS_2 > Ni_3S_2/MoS_2. A smaller arc radius indicates lower electrical impedance [42,43], which suggests more effective carrier transport. The heterostructure indeed exhibits improved transport of photogenerated charge carriers because the Nyquist plot of the Ni_3S_2/MoS_2 photocatalyst exhibits the smallest arc radius. Fig. 5(d) shows the photocurrent–time curves under dark and visible-light conditions in an on-and-off cycle mode. All of the samples quickly exhibited a photocurrent response as they are irradiated with light. Within the first few seconds of illumination, a slight photocurrent decay for each simple appeared in the diagram. Perhaps it is caused though the concentrated gradient exists at the interface of the semiconductors (Ni_3S_2/MoS_2, MoS_2, Ni_3S_2) and electrolyte (0.5 mol L^{-1} Na_2SO_4 solution), while the system is not stirring [44]. Overall the samples, including Ni_3S_2/MoS_2 heterostructure, single MoS_2 and Ni_3S_2, exhibit stable photocurrent response finally during the photoelectrochemical test process. Besides, the heterostructure shows higher photocurrent response intensity than that of single MoS_2 and Ni_3S_2, which is consistent with that the Ni_3S_2/MoS_2 heterostructure exhibits the best photocatalytic hydrogen evolution performance. Thus, the separation efficiency of electron–hole pairs is distinctly enhanced by the abundant interfaces of the Ni_3S_2/MoS_2 heterostructure. This phenomenon can be explained by the energy-level alignment of the semiconductor band states. The staggered gap [45] of Ni_3S_2 and MoS_2 leads to a built-in field at the junction interface, driving the photoexcited electron–hole pairs to separate and transport to the respective sides of the heterojunction [46]. The electrons preferentially transfer from the conduction band of Ni_3S_2 to the conduction band of MoS_2, accelerating the separation of photoexcited electron–hole pairs and facilitating the transport of electrons to the active sites of MoS_2 for photocatalytic hydrogen evolution (Fig. 5(e)). In general, the interlaced hybrid structure with a high carrier concentration reduces carrier recombination and promotes the migration of electrons, resulting in spatial separation of electron–hole pairs.

4. Conclusion

In summary, an interlaced Ni_3S_2/MoS_2 heterostructure with abundant intimate interfacial contacts was synthesized via a hydrothermal method. Ni foam was sulfurized in a CVD system, leading to a porous Ni_3S_2 scaffold; Ni_3S_2 nanosheets grew at certain oblique angle and were interconnected. Then, MoS_2 grew via a hydrothermal method and contacted with the Ni_3S_2 intimately. The Ni_3S_2/MoS_2 heterostructure exhibited an extended optical absorption region from 300 to 800 nm. PL spectra and photoelectrochemical measurements revealed that the interlaced Ni_3S_2/MoS_2 structure indeed reduced carrier recombination, accelerated the separation of photoexcited electron–hole pairs in the semiconductors, and facilitated the transport of carriers. Consequently, the Ni_3S_2/MoS_2 heterostructure showed a larger rate of hydrogen evolution (540.75 μmol g^{-1} h^{-1}) than the pure Ni_3S_2 (94.67 μmol g^{-1} h^{-1}) and MoS_2 (138.88 μmol g^{-1} h^{-1}). Moreover, the interlaced Ni_3S_2/MoS_2 heterostructure itself is a promising photocatalyst because of its high natural abundance and low cost. Our research provides a useful approach to improving photocatalytic performance.

Acknowledgments

This research is supported by Basic Research Fund for Free Exploration (JCYJ20170815161437298), the National Natural Science Foundation of China (51571166, 61505167 and 61701003), and the National Natural Science Fund for Excellent Young Scholars (No. 61722101). We also thank the support of Shaanxi Young Stars in Science and technology (2017KJXX-18), the Research Fund of the State Key Laboratory of Solidification Processing (NWPU) (Grant No. 147-QZ-2016), The Research Fund of Key Laboratory of Materials Physics, Institute of Solid State Physics, CAS (2016KLMP04), and the Key Scientific and Technological Team from Shaanxi Province (No. 2015KCT-12). This work was also supported by the Introduction Project of High-Level Talent in Anhui University (No. J01001320) and State Key Laboratory of Silicate Materials for Architectures, Wuhan University of Technology (No. SYSJJ2017-02).

References

[1] A. Landman, H. Dotan, G.E. Shter, M. Wullenkord, A. Houaijia, A. Maljusch, G.S. Grader, A. Rothschild, Photoelectrochemical water splitting in separate oxygen and hydrogen cells, Nat. Mater. 16 (2017) 646–651.
[2] Q. Wang, T. Hisatomi, Q. Jia, H. Tokudome, M. Zhong, C. Wang, Z. Pan, T. Takata, M. Nakabayashi, N. Shibata, Y. Li, I.D. Sharp, A. Kudo, T. Yamada, K. Domen, Scalable water splitting on particulate photocatalyst sheets with a solar-to-hydrogen energy conversion efficiency exceeding 1, Nat. Mater. 15 (2016) 611–615.
[3] J. Zhang, T. Wang, D. Pohl, B. Rellinghaus, R. Dong, S. Liu, X. Zhuang, X. Feng, Interface engineering of MoS_2/Ni_3S_2 heterostructures for highly enhanced electrochemical overall-water-splitting activity, Angew. Chem. Int. Ed. 55 (2016) 6702–6707.
[4] X. Li, J. Zhu, B. Wei, Hybrid nanostructures of metal/two-dimensional nanomaterials for plasmon-enhanced applications, Chem. Soc. Rev. 45 (2016) 3145–3187.
[5] M.Z. Rahman, C.W. Kwong, K. Davey, S.Z. Qiao, 2D phosphorene as a water splitting photocatalyst: fundamentals to applications, Energy Environ. Sci. 9 (2016) 709–728.
[6] X. Li, X. Ren, F. Xie, Y. Zhang, T. Xu, B. Wei, W.C.H. Choy, High-performance organic solar cells with broadband absorption enhancement and reliable reproducibility enabled by collective plasmonic effects, Adv. Opt. Mater. 3 (2015) 1220–1231.
[7] X. Li, X. Ren, Y. Zhang, W.C.H. Choy, B. Wei, An all-copper plasmonic sandwich system obtained through directly depositing copper NPs on a CVD grown graphene/copper film and its application in SERS, Nanoscale 7 (2015) 11291–11299.
[8] T. Daeneke, N. Dahr, P. Atkin, R.M. Clark, C.J. Harrison, R. Brkljaca, N. Pillai, B.Y. Zhang, A. Zavabeti, S.J. Ippolito, K.J. Berean, J.Z. Ou, M.S. Strano, K. Kalantar-Zadeh, Surface water dependent properties of sulfur-rich molybdenum sulfides: electrolyteless gas phase water splitting, ACS Nano 11 (2017) 6782–6794.
[9] J. Shi, R. Tong, X. Zhou, Y. Gong, Z. Zhang, Q. Ji, Y. Zhang, Q. Fang, L. Gu, X. Wang, Z. Liu, Y. Zhang, Temperature-mediated selective growth of MoS_2/WS_2 and WS_2/MoS_2 vertical stacks on Au foils for direct photocatalytic applications, Adv. Mater. 28 (2016) 10664–10672.
[10] Z. Qin, Y. Chen, Z. Huang, J. Su, Z. Diao, L. Guo, Composition-dependent catalytic activities of noble-metal-free NiS/$Ni_3S_4$for hydrogen evolution reaction, Phys. Chem. C 120 (2016) 14581–14589.
[11] Z. Sun, H. Chen, L. Zhang, D. Lu, P. Du, Enhanced photocatalytic H_2 production on cadmium sulfide photocatalysts using nickel nitride as a novel cocatalyst, J. Mater. Chem. A 4 (2016) 13289–13295.
[12] J. Zhang, L. Qi, J. Ran, J. Yu, S.Z. Qiao, Ternary NiS/$Zn_xCd_{1-x}S$/reduced graphene oxide nanocomposites for enhanced solar photocatalytic H_2 production activity, Adv. Energy Mater. 4 (2014), 1301925.
[13] P. Luo, H. Zhang, L. Liu, Y. Zhang, J. Deng, C. Xu, N. Hu, Y. Wang, Targeted synthesis of unique nickel sulfide (NiS, NiS_2) microarchitectures and the applications for the enhanced water splitting system, ACS Appl. Mater. Interfaces 9 (2017) 2500–2508.
[14] X. Liu, X. Liang, P. Wang, B. Huang, X. Qin, X. Zhang, Y. Dai, Highly efficient and noble metal-free NiS modified $Mn_xCd_{1-x}S$ solid solutions with enhanced photocatalytic activity for hydrogen evolution under visible light irradiation, Appl. Catal. B Environ. 203 (2017) 282–288.
[15] J. Yuan, J. Wen, Y. Zhong, X. Li, Y. Fang, S. Zhang, W. Liu, Enhanced

photocatalytic H_2 evolution over noble-metal-free NiS cocatalyst modified CdS nanorods/g-C_3N_4 heterojunctions, J. Mater. Chem. A 3 (2015) 18244–18255.
[16] L.L. Feng, G. Yu, Y. Wu, G.D. Li, H. Li, Y. Sun, T. Asefa, W. Chen, X. Zou, High-index faceted Ni_3S_2 nanosheet arrays as highly active and ultrastable electrocatalysts for water splitting, J. Am. Chem. Soc. 137 (2015) 14023–14026.
[17] Y. Tian, F.P. Garcia de Arquer, C.T. Dinh, G. Favraud, M. Bonifazi, J. Li, M. Liu, X. Zhang, X. Zheng, M.G. Kibria, S. Hoogland, D. Sinton, E.H. Sargent, A. Fratalocchi, Enhanced solar-to-hydrogen generation with broadband epsilon-near-zero nanostructured photocatalysts, Adv. Mater. 29 (2017), 1701165.
[18] S. Bai, L. Yang, C. Wang, Y. Lin, J. Lu, J. Jiang, Y. Xiong, Boosting photocatalytic water splitting: interfacial charge polarization in atomically controlled core-shell cocatalysts, Angew. Chem. Int. Ed. 54 (2015) 14810–14814.
[19] K.C. Hung, Y.H. Lai, T.W. Lin, Enhancement of photocatalytic hydrogen formation under visible illumination by integrating plasmonic Au nanoparticles with a strongly catalytic Ni_3S_2/carbon nanotube composite, Catal. Sci. Technol. 6 (2016) 4020–4026.
[20] B. Han, S. Liu, N. Zhang, Y.J. Xu, Z.R. Tang, One-dimensional CdS@MoS_2 core-shell nanowires for boosted photocatalytic hydrogen evolution under visible light, Appl. Catal. B Environ. 202 (2017) 298–304.
[21] Q. Liu, Q. Shang, A. Khalil, Q. Fang, S. Chen, Q. He, T. Xiang, D. Liu, Q. Zhang, Y. Luo, L. Song, In situ integration of a metallic 1T-MoS_2/CdS heterostructure as a means to promote visible-light-driven photocatalytic hydrogen evolution, ChemCatChem 8 (2016) 2614–2619.
[22] W. Fang, J. Liu, D. Yang, Z. Wei, Z. Jiang, W. Shangguan, Effect of surface self-heterojunction existed in $Bi_xY_{1-x}VO_4$ on photocatalytic overall water splitting, ACS Sustain. Chem. Eng. 5 (2017) 6578–6584.
[23] J. Low, J. Yu, M. Jaroniec, S. Wageh, A.A. Al-Ghamdi, Heterojunction photocatalysts, Adv. Mater. 29 (2017), 1601694.
[24] S. Guo, X. Li, J. Zhu, T. Tong, B. Wei, Au NPs@ MoS_2 sub-micrometer sphere-ZnO nanorod hybrid structures for efficient photocatalytic hydrogen evolution with excellent stability, Small 12 (2016) 5692–5701.
[25] X. Li, S. Guo, C. Kan, J. Zhu, T. Tong, S. Ke, W.C.H. Choy, B. Wei, Au Multimer@ MoS_2 hybrid structures for efficient photocatalytical hydrogen production via strongly plasmonic coupling effect, Nano Energy 30 (2016) 549–558.
[26] W. Zhou, Z. Yin, Y. Du, X. Huang, Z. Zeng, Z. Fan, H. Liu, J. Wang, H. Zhang, Synthesis of few-layer MoS_2 nanosheet-coated TiO_2 nanobelt heterostructures for enhanced photocatalytic activities, Small 9 (2013) 140–147.
[27] C. An, J. Feng, J. Liu, G. Wei, J. Du, H. Wang, S. Jin, J. Zhang, NiS nanoparticle decorated MoS_2 nanosheets as efficient promoters for enhanced solar H_2 evolution over $Zn_xCd_{1-x}S$ nanorods, Inorg. Chem. Front. 4 (2017) 1042–1047.
[28] Z. Zhang, Q. Wang, C. Zhao, S. Min, X. Qian, One-step hydrothermal synthesis of 3D petal-like Co_9S_8/RGO/Ni_3S_2 composite on nickel foam for high-performance supercapacitors, ACS Appl. Mater. Interfaces 7 (2015) 4861–4868.
[29] T. An, Y. Wang, J. Tang, W. Wei, X. Cui, A.M. Alenizi, L. Zhang, G. Zheng, Interlaced NiS_2–MoS_2 nanoflake-nanowires as efficient hydrogen evolution electrocatalysts in basic solutions, J. Mater. Chem. A 4 (2016) 7549–7554.
[30] Y.J. Yuan, H.W. Lu, Z.T. Yu, Z.G. Zou, Noble-metal-free molybdenum disulfide cocatalyst for photocatalytic hydrogen production, ChemSusChem 8 (2015) 4113–4127.
[31] F.X. Xiao, J. Miao, H.Y. Wang, H. Yang, J. Chen, B. Liu, Electrochemical construction of hierarchically ordered CdSe-sensitized TiO_2 nanotube arrays: towards versatile photoelectrochemical water splitting and photoredox applications, Nanoscale 6 (2014) 6727–6737.
[32] C. Zhe, A. Harry, L. Meilin, Raman spectroscopy of nickel sulfide Ni_3S_2, J. Phys. Chem. C 111 (2007) 17997–18000.
[33] X. Sun, H. Deng, W. Zhu, Z. Yu, C. Wu, Y. Xie, Interface engineering in two-dimensional heterostructures: towards an advanced catalyst for ullmann couplings, Angew. Chem. Int. Ed. 55 (2016) 1704–1709.
[34] X. Wang, G. Liu, Z.G. Chen, F. Li, L. Wang, G.Q. Lu, H.M. Cheng, Enhanced photocatalytic hydrogen evolution by prolonging the lifetime of carriers in ZnO/CdS heterostructures, Chem. Commun. 23 (2009) 3452–3454.
[35] W. Zhao, Y. Liu, Z. Wei, S. Yang, H. He, C. Sun, Fabrication of a novel p–n heterojunction photocatalyst n-$BiVO_4$@p-MoS_2 with core–shell structure and its excellent visible-light photocatalytic reduction and oxidation activities, Appl. Catal. B Environ. 185 (2016) 242–252.
[36] S. Iqbal, Z. Pan, K. Zhou, Enhanced photocatalytic hydrogen evolution from in situ formation of few-layered MoS_2/CdS nanosheet-based van der Waals heterostructures, Nanoscale 9 (2017) 6638–6642.
[37] L. Yang, S. Guo, X. Li, Au nanoparticles@MoS_2 core-shell structures with moderate MoS2 coverage for efficient photocatalytic water splitting, J. Alloys Compd. 706 (2017) 82–88.
[38] S. Wang, X. Li, T. Tong, J. Han, Y. Zhang, J. Zhu, Z. Huang, W.C.H. Choy, Sequential processing: spontaneous improvements in film quality and interfacial engineering for efficient perovskite solar cells, Solar RRL (2018), https://doi.org/10.1002/solr.201800027.
[39] H.L. Shi, H. Pan, Y.W. Zhang, B.I. Yakobson, Quasiparticle band structures and optical properties of strained monolayer MoS_2 and WS_2, Phys. Rev. B 87 (2013), 155304.
[40] Q.L. Song, H.B. Yang, Y. Gan, C. Gong, C.M. Li, Evidence of harvesting electricity by exciton recombination in an n-n type solar cell, J. Am. Chem. Soc. 132 (2010) 4554–4555.
[41] Q.L. Song, C.M. Li, M.B. Chan-Park, Exciton dissociation in organic light emitting diodes at the donor-acceptor interface, Phys. Rev. Lett. 98 (2007) 176403.
[42] L. Zhao, J. Jia, Z. Yang, J. Yu, A. Wang, Y. Sang, W. Zhou, H. Liu, One-step synthesis of CdS nanoparticles/MoS_2 nanosheets heterostructure on porous molybdenum sheet for enhanced photocatalytic H_2 evolution, Appl. Catal. B Environ. 210 (2017) 290–296.
[43] L. Yang, W. Zhou, J. Lu, D. Hou, Y. Ke, G. Li, Z. Tang, X. Kang, S. Chen, Hierarchical spheres constructed by defect-rich MoS_2/carbon nanosheets for efficient electrocatalytic hydrogen evolution, Nano Energy 22 (2016) 490–498.
[44] Y. Liu, H. He, J. Li, W. Li, Y. Yang, Y. Li, Q. Chen, ZnO nanoparticle-functionalized WO_3 plates with enhanced photoelectrochemical properties, RSC Adv. 5 (2015) 46928.
[45] B. Busupalli, K. Date, S. Datar, B.L.V. Prasad, Preparation of Ni_3S_2 and Ni_3S_2–Ni nanosheets via solution based processes, Cryst. Growth Des. 15 (2015) 2584–2588.
[46] Y. Bai, T. Chen, P. Wang, L. Wang, L. Ye, Bismuth-rich $Bi_4O_5X_2$ (X=Br, and I) nanosheets with dominant {101} facets exposure for photocatalytic H_2 evolution, Chem. Eng. J. 304 (2016) 454–460.